Solar Phys (2009) 260: 347–361
DOI 10.1007/s11207-009-9457-z

Electron-Temperature Maps of the Low Solar Corona: ISCORE Results from the Total Solar Eclipse of 29 March 2006 in Libya

Nelson L. Reginald · O.C. St. Cyr · Joseph M. Davila · Douglas M. Rabin · Madhulika Guhathakurta · Donald M. Hassler

Received: 15 December 2008 / Accepted: 17 September 2009 / Published online: 15 October 2009

Abstract We conducted an experiment in conjunction with the total solar eclipse of 29 March 2006 in Libya that measured the coronal intensity through two filters centered at 3850 Å and 4100 Å with bandwidths of ≈40 Å. The purpose of these measurements was to obtain the intensity ratio through these two filters to determine the electron temperature. The instrument, *Imaging Spectrograph of Coronal Electrons* (ISCORE), consisted of an eight inch, f/10 Schmidt Cassegrain telescope with a thermoelectrically-cooled CCD camera at the focal plane. Results show electron temperatures of 10^5 K close to the limb to 3×10^6 K at $1.3R_{\odot}$. We describe this novel technique, and we compare our results to other relevant measurements. This technique could be easily implemented on a space-based platform using a coronagraph to produce global maps of the electron temperature of the solar corona.

Keywords Solar corona · K-corona · Electron temperature · Solar wind · Eclipse science and spectrograph

1. Introduction

For more than 50 years the solar corona has intrigued researchers with its physical properties of a million-degree temperature together with the energy to accelerate the solar wind

N.L. Reginald (✉)
The Catholic University of America at NASA's Goddard Space Flight Center, MC 671, Greenbelt, MD 20771, USA
e-mail: Nelson.L.Reginald@nasa.gov

O.C. St. Cyr · J.M. Davila · D.M. Rabin
MC 671, NASA's Goddard Space Flight Center, Greenbelt, MD 20771, USA

M. Guhathakurta
NASA Headquarters, 300 E Street SW, Washington, DC 20024, USA

D.M. Hassler
Southwest Research Institute, 1050 Walnut Street, Suite 400, Boulder, CO 80302, USA

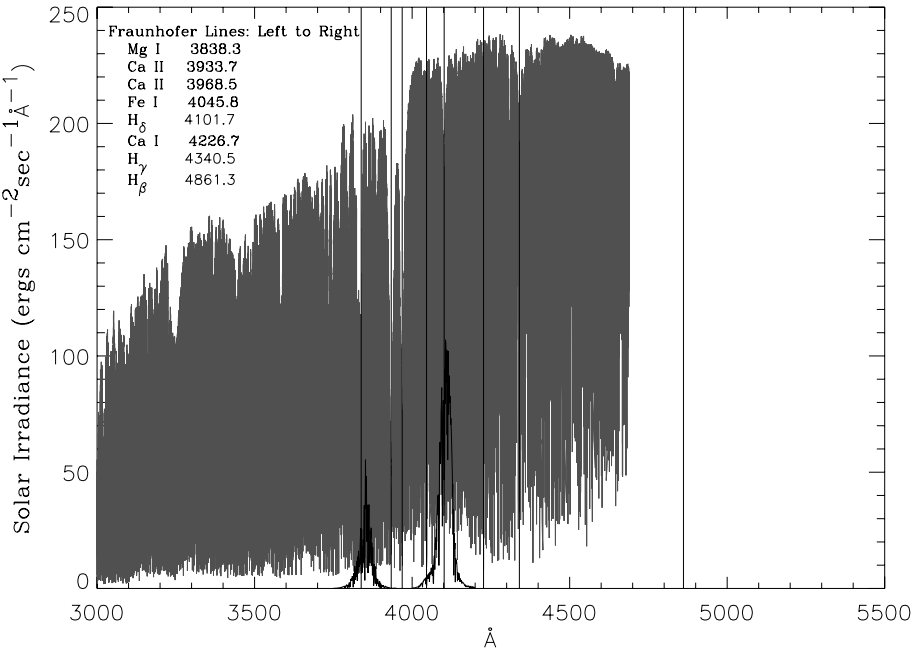

Figure 1 Solar photospheric spectrum in the visible wavelength region, which is incident on the coronal electrons. This spectrum was obtained with a ground-based Fourier transform spectrometer at the McMath – Pierce Solar Telescope at Kitt Peak, Arizona and is corrected for wavelength-dependent absorption in the Earth's atmosphere (Kurucz *et al.*, 1984). Also shown are the profiles of the two filters centered at 3850 Å and 4100 Å. The vertical lines show the locations of the Fraunhofer lines listed in the figure.

to supersonic speeds. Emission lines from highly-charged Fe ions discovered during total eclipses were the first indication of temperatures above the 5000° photosphere, and it led researchers to examine coronal temperatures and flow speeds using Doppler-shifted emission from Fe and other coronal ions. Examples include Habbal, Esser, and Arndt (1993), Guhathakurta, Fisher, and Altrock (1993), Brosius *et al.* (1997), Mason *et al.* (1997), Kohl *et al.* (1995), Doppler dimming of ultraviolet spectral features (*e.g.*, Strachan *et al.*, 1993), and visible imaging spectroscopy (*e.g.*, Brueckner *et al.*, 1995).

Based on a technique first proposed by Cram (1976), and extended by Reginald and Davila (2000), we have obtained coronal diagnostics on the thermal electron temperature and its flow speed by observing the Thomson-scattered emission from coronal electrons. Earlier attempts using electron-based measurements include Grall *et al.* (1996), using interplanetary radio scintillation measurements, and Fineschi *et al.* (1998), using Ly α profiles obtained from observations through the *Ultraviolet Coronagraph Spectrometer* (UVCS) onboard the *Solar and Heliospheric Observatory* (SOHO). Ichimoto *et al.* (1996) obtained a measurement also based on electron scattering. Reginald *et al.* (2003) reported spectroscopic measurements at several locations in the K-corona from measurements obtained during the 2001 eclipse in Zambia.

The K-corona, seen around the solar limb during an eclipse, is due to Thomson scattering of photospheric light off the coronal electrons. Although the photospheric spectrum, as shown in Figure 1, contains millions of absorption lines, including conspicuous Fraunhofer lines, the modeled spectrum that results from scattering off the coronal electrons is very

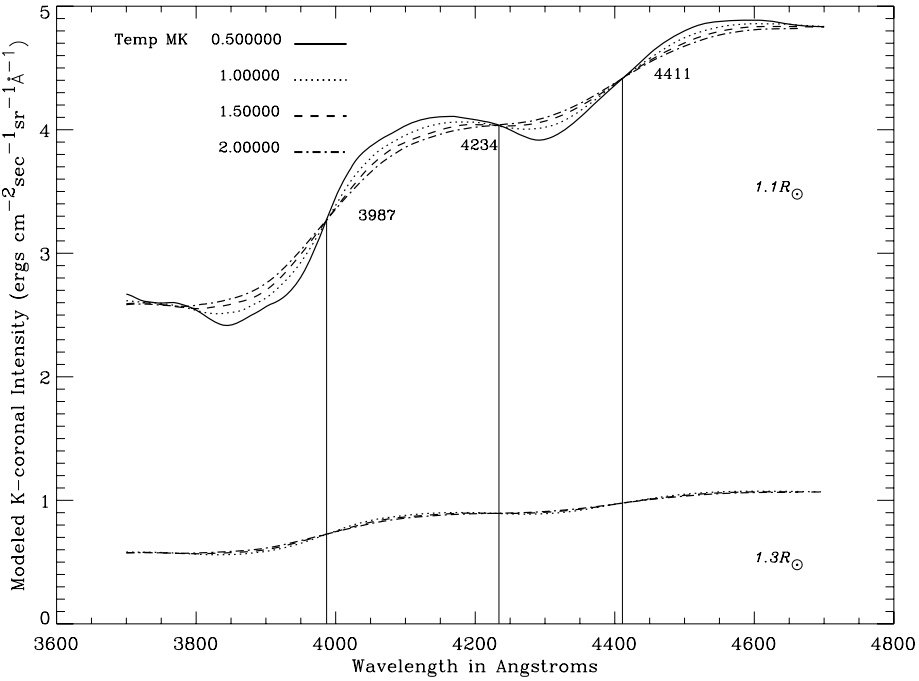

Figure 2 Theoretically modeled K-coronal spectrum at lines of sight at $1.1R_\odot$ and $1.3R_\odot$ for thermal-electron temperatures of 0.5, 1.0, 1.5, and 2.0 MK. The temperature insensitive nodes are at 3987, 4234, and 4411 Å.

smooth, as shown in Figure 2. This is a result of the high thermal velocities of the coronal electrons, which causes the total obliteration of the absorption lines in the incident photospheric spectrum to produce a smooth spectrum through thermal Doppler broadening. The only remaining features are slight depressions at wavelengths that once contained the deep Fraunhofer lines such as the Ca II K and H lines at 3933.7 Å and 3968.5 Å. Figure 2 shows the theoretically modeled Thomson-scattered K-coronal spectrum for coronal electron temperatures of 0.5, 1.0, 1.5, and 2.0 MK at lines of sight at $1.1R_\odot$ and $1.3R_\odot$. The temperature insensitive nodes in Figure 2 were initially noted by Cram (1976) and these modeled nodal locations are remarkably maintained with coronal height. It is clearly evident from Figure 2 that the absorption features of the photospheric radiation shown in Figure 1 have been smoothed by the thermal Doppler-broadening process leaving only shallow depressions at wavelengths that once contained deep Fraunhofer lines. For example, the Doppler broadening that results in filling the valleys and flattening the peaks in the incident photospheric spectrum broadens the photospheric radiation at 4000 Å by $\approx$70 Å in a 1 MK coronal plasma.

In producing the modeled K-coronal spectrum along any given line of sight in the corona, we assumed a spherically-symmetric corona based on the electron-density profile given by Baumbach (1937), which was based on photometric data from ten eclipses dating from 1905 to 1929. This density profile was confirmed by November and Koutchmy (1996) when they had the unique opportunity of obtaining the same photometric data through the use of the 3.6-m Canada – Franch – Hawaii Telescope (CFHT) located on Mauna Kea, Hawaii during the total solar eclipse on 11 July 1991 whose path crossed that telescope.

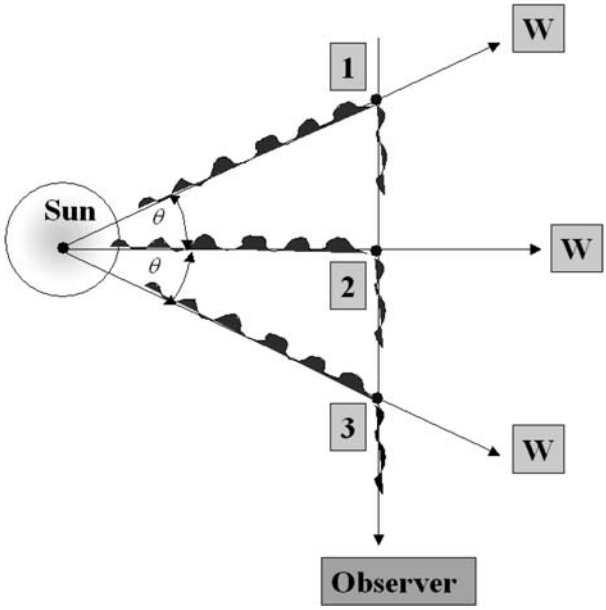

Figure 3 The red-shifting of the K-coronal spectrum due to the outward bulk flow speed of the coronal electrons.

If not for the time constraint associated with a solar eclipse, the electron density could have been obtained at the time of the experiment by the measurement of the coronal intensity through three polarizing angles.

We then integrated the contribution by all of the electrons located along each line of sight through the Thomson-scattering process. We also allowed for the angular dependence of the Thomson-scattering process together with the effect of a wavelength-dependent limb-darkening coefficient on the incident photospheric radiation from different parts of the Sun on the coronal electrons located along that line of sight. Also assumed were a Maxwellian velocity distribution for the coronal electrons and an isothermal and symmetric corona.

The hot solar corona is not static, but instead the coronal electrons flow away from the Sun as solar wind. Therefore the formalism of Cram (1976) was extended to allow for a Maxwellian distribution with a bulk flow speed, as discussed in Reginald and Davila (2000). As a consequence, the outward-propagating electron plasma would observe a red-shifted photosphere in the reference frame of the electrons, with the amount of red-shift proportional to the outward flow speed. The amount of red-shift observed by these electrons will be preserved in wavelength in the Thomson-scattering process due to its wavelength independence in the rest frame of the electrons. This yields a remarkable difference between Doppler measurements of line emission and the Thomson-scattering process where the latter allows for red-shifts even when the electron velocity is transverse to the line of sight.

Figure 3 is a schematic to illustrate this point. Here the coronal electrons are shown at equal distance, from the point where the line of sight intersects the plane of the sky, in front and behind the solar limb. The coronal electrons at the locations numbered 1, 2, and 3 are all moving away from the Sun at some speed w. Hence they are all seeing a red-shifted photosphere in the reference frame of the electrons. Some portion of this incident photospheric radiation is Thomson-scattered by these electrons located at positions 1, 2, and 3 in the direction towards the observer. Also this scattered radiation is red shifted in proportion to the bulk flow speeds of these electrons since the Thomson-scattering process

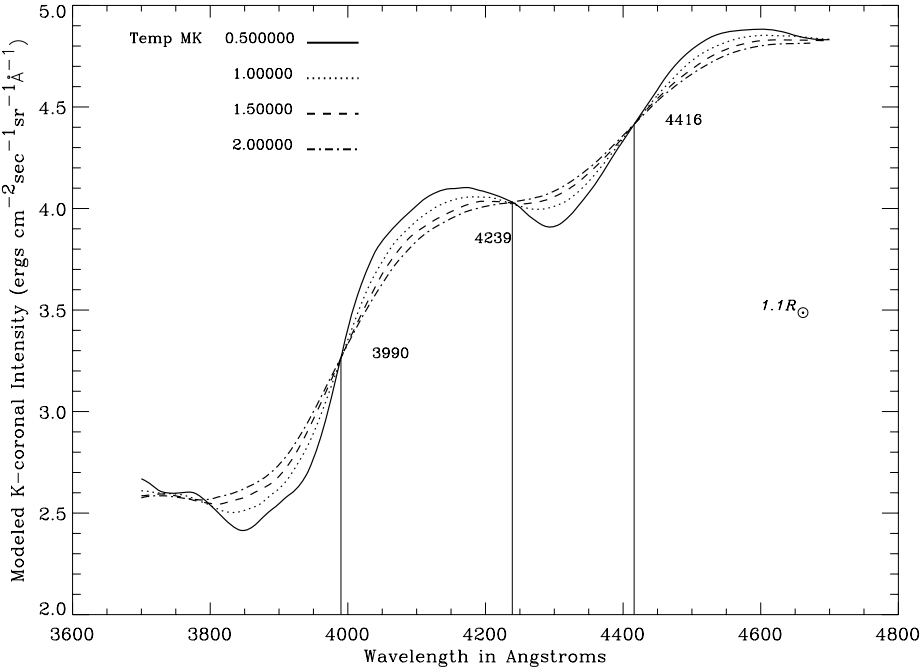

Figure 4 Modeled K-coronal spectral intensity as a function of wavelength for isothermal coronal temperatures of 0.5, 1.0, 1.5, and 2.0 MK, and an electron bulk flow speed of 400 km s^{-1}, for a line of sight at 1.1$R_\odot$. The temperature insensitive nodes are at 3990, 4239, and 4416 Å.

itself is wavelength independent. However the electrons located at positions 1 and 3 also have a velocity component that is directed away from and towards the observer, respectively. Therefore the Thomson-scattered radiation by electrons at positions 1 and 3 are additionally red and blue shifted, respectively, with the net results from all of the electrons located along the line of sight of the observer being a red-shifted K-coronal spectrum.

Reginald (2000) incorporated the effects of electron flow speed into the modeling of the K-coronal spectrum and found that when the contributions of all the electrons located along a given line of sight are summed then the entire K-coronal spectrum shown in Figure 2 is slightly red shifted in proportion to the electron flow speed. Figure 4 and Figure 5 show the modeled K-coronal spectrum, for coronal electron temperatures of 0.5, 1.0, 1.5, and 2.0 MK with bulk flow speeds of 400 km s^{-1} and 800 km s^{-1}, respectively, along a line of sight at 1.1$R_\odot$.

Therefore for a given line of sight, measuring the K-coronal spectrum can yield both the electron temperature and its bulk flow speed, determined by comparing models that fit the shape of the measured K-coronal spectrum. Results from such an experiment were described by Reginald *et al.* (2003).

To obtain temperature maps of the corona, we have followed the following procedure: From Figure 2 we note that the intensities for different coronal electron temperatures have the largest differences at wavelength positions such as 3850 Å and 4100 Å, which we call "anti-nodes". We now calculate the intensity ratios from Figure 2 at the two anti-nodes centered at wavelength positions 3850 Å and 4100 Å, which we call "temperature-sensitive intensity ratios". By calculating this "temperature-sensitive intensity ratio" for different

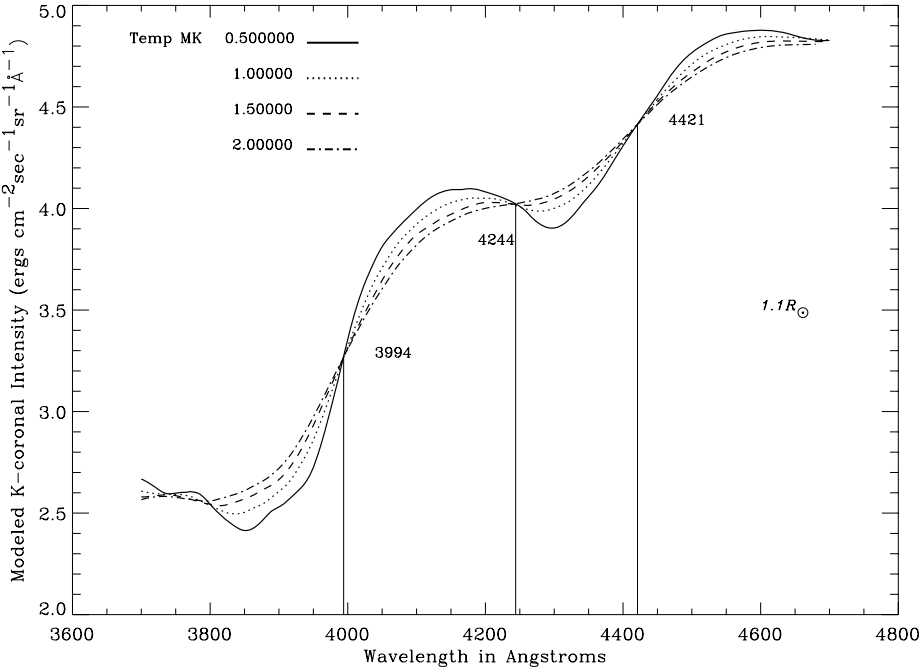

Figure 5 Modeled K-coronal spectral intensity as a function of wavelength for isothermal coronal temperatures of 0.5, 1.0, 1.5, and 2.0 MK, and an electron bulk flow speed of 800 km s^{-1}, for a line of sight at 1.1 $R_\odot$. The temperature insensitive nodes are at 3994, 4244, and 4421 Å.

K-coronal models with different electron temperatures, we can produce a temperature index that would chart the "temperature-sensitive intensity ratio" *versus* "electron temperature". Through modeling we have noticed that the "temperature-sensitive intensity ratio" is maintained with different coronal heights and bulk flow speeds for a given coronal electron temperature for the coronal plasma. As an example, the "temperature-sensitive intensity ratio" for a K-coronal model with a given electron temperature would be remarkably maintained in Figures 2, 4, and 5. In the ISCORE experiment, we have utilized the above technique to determine the electron temperature on a pixel-by-pixel basis through the measurements of the "temperature-sensitive intensity ratios" of the individual pixels.

The profiles of the two filters centered at the two anti-nodes pertaining to this experiment are shown in Figure 1. Figure 6 shows the modeled "temperature-sensitive intensity ratios" based on the filter profiles shown in Figure 1 applied on K-coronal models with electron temperatures close to 0.0 MK to 10.0 MK and bulk flow speeds ranging from 0–900 km s^{-1}. Figure 6 indicates a unique profile that can be used to determine the electron temperature through the measurement of the "temperature-sensitive intensity ratio" on a pixel-by-pixel basis. In a like manner, it was shown by Reginald and Davila (2000) that the bulk flow speed could be determined on a pixel-by-pixel basis through the measurement of the coronal intensity through four filters centered at 4233 Å, 4100 Å, 3987 Å, and 3850 Å where the intensity ratio between 4233 Å and 3987 Å is called the "wind-sensitive intensity ratio".

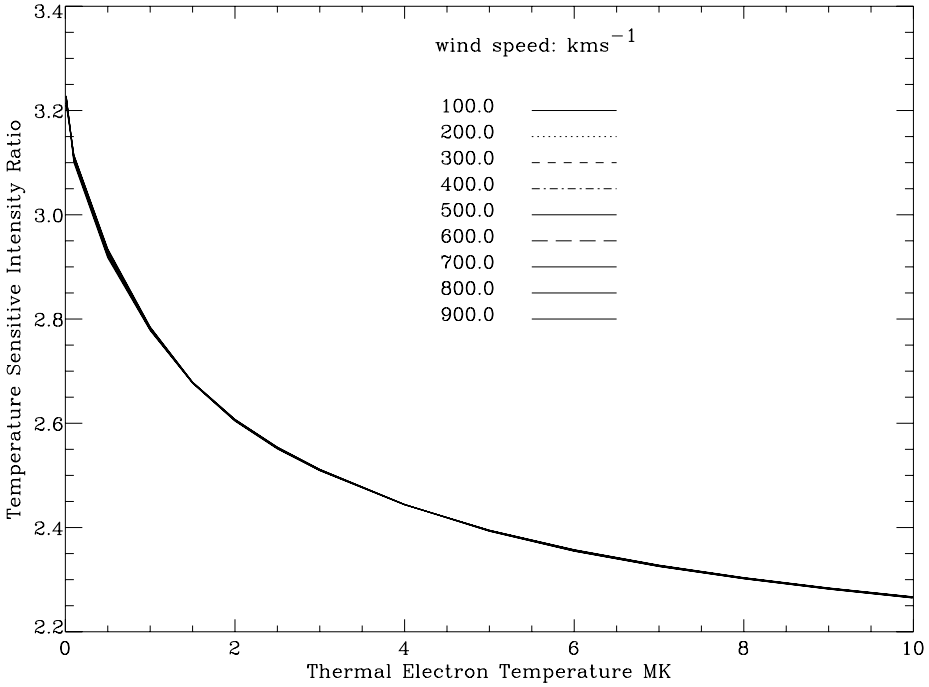

Figure 6 Modeled "temperature-sensitive intensity ratios" using two filter profiles shown in Figure 1 on modeled K-coronal profiles, such as shown in Figure 2, with various electron temperatures and bulk flow speeds. The measured "extraterrestrial coronal intensity ratios" $I_{\mathrm{E}}^{\mathrm{C}}(\lambda)$ will be matched with modeled "temperature-sensitive intensity ratios" (y axis) on a pixel-by-pixel basis to determine the electron temperature (x-axis) corresponding to that pixel.

2. Data Collection

The telescope used to obtain the solar coronal images at the total eclipse was an 8-inch, f/10 Schmidt Cassegrain Meade™ telescope along with a f/3.3 focal reducer. This was coupled to a computer-operated filter wheel which contained the 3850 Å and 4100 Å filters and followed by a back-thinned 512 × 512, 24 μm square pixel, thermoelectrically-cooled Apogee™ CCD camera at the focal plane of the telescope. The filters were obtained from the Andover™ Corp, who also provided transmission curves that we verified independently.

The details of the eclipse can be found in Espenak and Anderson (2004), and a description of the 2006 eclipse expedition was presented by St. Cyr *et al.* (2007). Here we simply note the date (29 March 2006); the duration (204 seconds), and the location (Libya's Sahara Desert).

In addition to taking solar coronal images during the eclipse, images of the solar photosphere were also taken, pre- and post-eclipse, using the 3850 Å and 4100 Å filters and a pinhole in the front aperture of the telescope. These images were used in the data analysis to account for the intensity attenuation associated with the Earth's atmosphere and transmission properties of the instrumental optics.

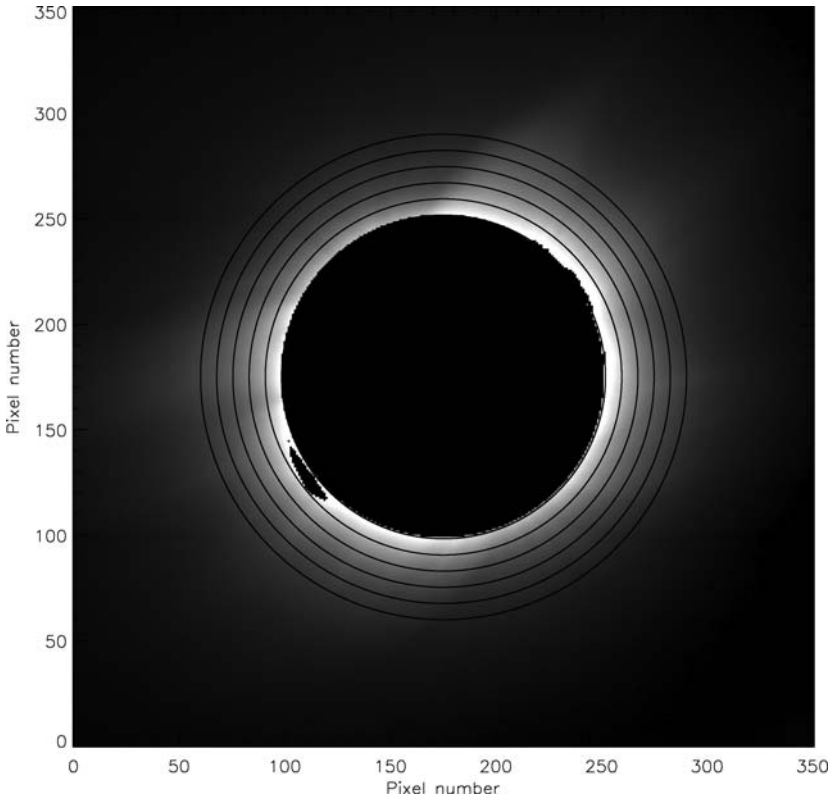

Figure 7 Coronal image taken using the 4100 Å filter during the 29 March 2006 totality in Libya. The duration of the exposure was 0.8 seconds. The filter profile is shown in Figure 1. The concentric circles are plotted in intervals of $0.1 R_{\odot}$ starting from $1.1 R_{\odot}$.

3. Data Analysis and Results

Figure 7 and Figure 8 show the coronal images taken through the 4100 Å and 3850 Å filters during the 29 March 2006 totality in Libya, respectively. Figure 9 shows the ratio of these two images. The central dark circular area is the Moon's shadow, and the jagged darkened areas at the limb are due to overexposed prominences. Figure 10 shows a high-resolution picture of the eclipse superimposed on Figure 9 to highlight the streamer structures and the location of the prominence that caused the inter-pixel bleeding in Figures 7 and 8. The high-resolution, white-light image is shown only for the above purpose and did not feature in any of the data analysis.

We have restricted our analysis to those pixels where the noise level is $< 1.0\%$, which corresponds to an uncertainty of ± 0.2 MK on the temperature measurements. The following steps were used to determine that noise level: the standard deviation for each pixel was calculated from "dark" images (*i.e.* with the shutter closed) with matching exposure times, which is considered as the random noise level for that pixel.

Since the dark image matching its exposure time was subtracted from each image, the random noise level for each pixel was then twice the standard deviation, thus accounting for the random noise in both the exposed and the dark images used in obtaining Figure 7 and Figure 8. Due to the lack of a calibration source, the statistical error was theoretically

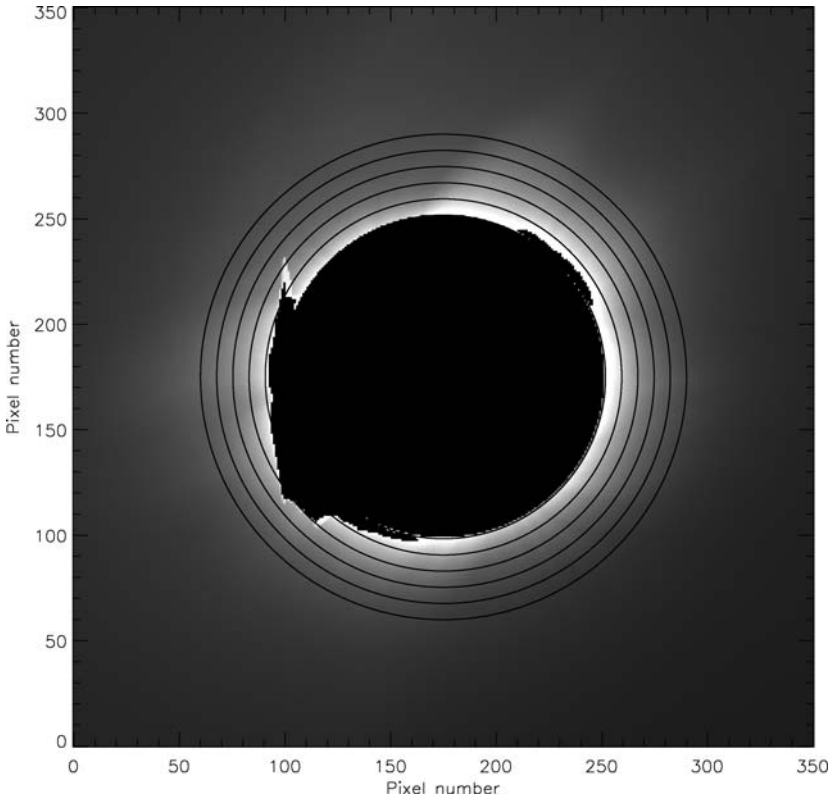

Figure 8 Coronal image taken using the 3850 Å filter during the 29 March 2006 totality in Libya. The duration of the exposure was eight seconds. The filter profile is shown in Figure 1. The concentric circles are plotted in intervals of $0.1R_{\odot}$ starting from $1.1R_{\odot}$.

determined to be the square of the Poisson error by assuming a Poisson distribution for the counts measured by each pixel, which is proportional to $\sqrt{N}$ where N is the number of electrons for that pixel. This value N for each pixel can be determined from the full-well depth of 300 000 electrons for 16-bit digitization for the camera used in this experiment. Based on this criterion the area of analysis in Figure 9 was restricted to the area shown in Figure 11.

We have followed the following steps in analyzing the data. First the images through the 3850 Å and 4100 Å filters were aligned through cross correlation of the coronal features and the individual images were divided by their exposure times. This is required because the Sun's position behind the Moon changed during exposures through the different filters. The images through the 4100 Å and 3850 Å filters as shown in Figures 7 and 8 were exposed for durations of 0.8 and 8.0 seconds, respectively. The shorter-wavelength filter had to be exposed for a longer duration due to its position in the blue that gets significantly attenuated by the Earth's atmosphere and instrumental optics. However some pixels were overexposed by a bright prominence as seen in Figure 8. Second, the 4100 Å image was divided by the 3850 Å image to produce the "terrestrial coronal intensity ratio" $I_{\mathrm{T}}^{\mathrm{C}}(\lambda)$ meaning the coronal intensity ratio as observed from the experimental location. Here the Moon's shadow regions, overexposed pixels, and pixels that had a noise level of $>$ than 1.0% were excluded. Third,

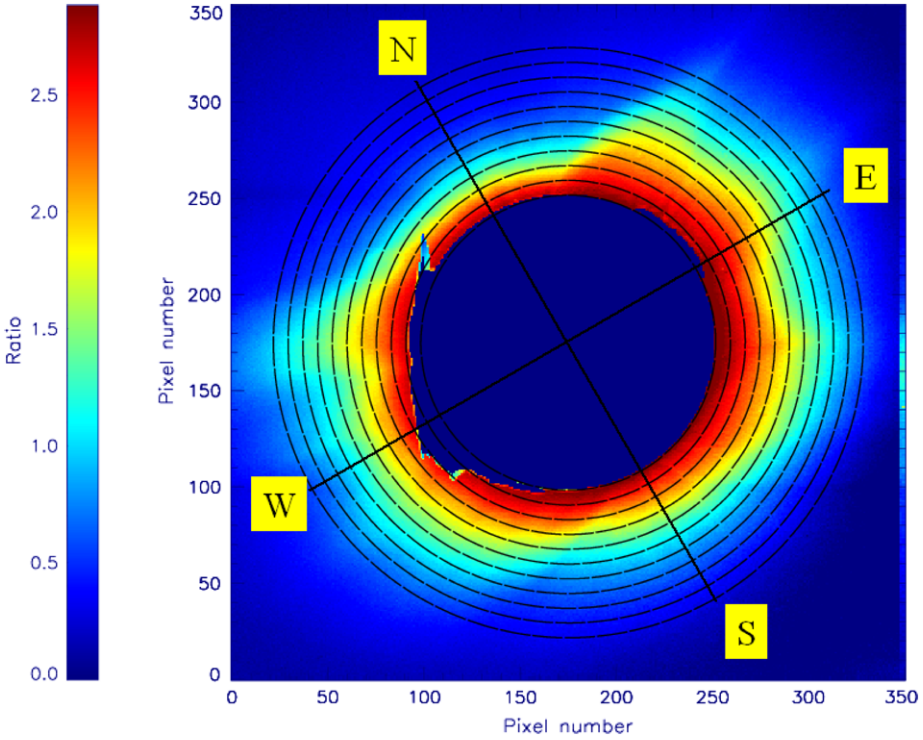

Figure 9 The ratio between the images shown in Figure 7 and Figure 8 after correcting them for intensity modulation by the Earth's atmosphere and instrumental optics. This figure represents the "extraterrestrial coronal intensity ratio" $I_{\mathrm{E}}^{\mathrm{C}}(\lambda)$. The concentric circles are plotted at intervals of $0.1\,R_{\odot}$ starting from $1.1\,R_{\odot}$.

this "terrestrial coronal intensity ratio" $I_{\mathrm{T}}^{\mathrm{C}}(\lambda)$ had to be transformed to an above the atmosphere "extraterrestrial coronal intensity ratio" $I_{\mathrm{E}}^{\mathrm{C}}(\lambda)$ to reflect the true coronal intensity ratio that is not affected by the attenuation of the intensity by the Earth's atmosphere and instrumental optics. For a given pixel, it is this measured "extraterrestrial coronal intensity ratio" $I_{\mathrm{E}}^{\mathrm{C}}(\lambda)$ that would be compared with the modeled "temperature-sensitive intensity ratio" in Figure 6 to determine the electron temperature for that pixel. This transformation from "terrestrial coronal intensity ratio" $I_{\mathrm{T}}^{\mathrm{C}}(\lambda)$ to "extraterrestrial coronal intensity ratio" $I_{\mathrm{E}}^{\mathrm{C}}(\lambda)$ was achieved by first taking images of the photosphere, pre- and post-eclipse, through the same two filters to obtain the "terrestrial photospheric intensity ratio" $I_{\mathrm{T}}^{\mathrm{P}}(\lambda)$. Here again each image of the photosphere was first divided by its exposure time. This was then compared with the modeled "extraterrestrial photospheric intensity ratio" $I_{\mathrm{E}}^{\mathrm{P}}(\lambda)$ derived by using the two filters profiles and the extraterrestrial photospheric spectrum shown in Figure 1. Any difference between the "terrestrial photospheric intensity ratio" $I_{\mathrm{T}}^{\mathrm{P}}(\lambda)$ and "extraterrestrial photospheric intensity ratio" $I_{\mathrm{E}}^{\mathrm{P}}(\lambda)$ for a given wavelength was assumed to represent the intensity attenuation attributed to Earth's atmosphere and instrumental optics at that wavelength. This correction was then applied to the "terrestrial coronal intensity ratio" $I_{\mathrm{T}}^{\mathrm{C}}(\lambda)$ to obtain "extraterrestrial coronal intensity ratio" $I_{\mathrm{E}}^{\mathrm{C}}(\lambda)$. This whole process can be represented by Equation (1) where I, C, P, T and E represent intensity, coronal, photosphere, terrestrial and extraterrestrial, respectively. The left-hand side of the equation that measures the "extraterrestrial coronal intensity ratio" $I_{\mathrm{E}}^{\mathrm{C}}(\lambda)$ on a pixel-by-pixel basis will be compared with

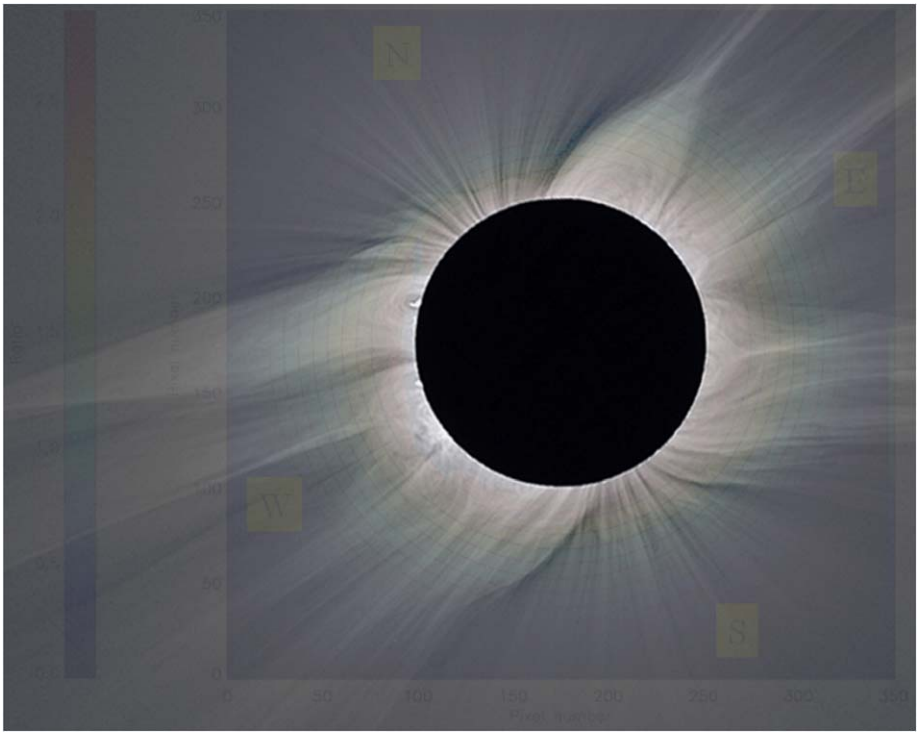

Figure 10 Figure 9 superimposed upon a high-resolution picture of the eclipse that shows detailed structures. This high-resolution white-light picture clearly shows the locations of the prominences that resulted in the inter-pixel bleeding in Figures 7 and 8. Courtesy of Miloslav Druckmuller, Peter Aniol.

modeled "temperature-sensitive intensity ratio" shown in Figure 6 to determine the electron temperature of the coronal plasma for the corresponding pixel.

We wish to mention again that the term "temperature-sensitive intensity ratio" (Figure 6, *y*-axis) is used to describe the modeled intensity ratios obtained by applying the 3850 Å and 4100 Å filter profiles on the modeled K-coronal spectra, which are theoretical ratios that are dependent on the coronal electron temperatures (Figure 6, *x*-axis) assumed for the coronal plasma in the K-coronal models. The temperature-dependent modeled "temperature-sensitive intensity ratio" that is applicable to a given pixel is the "extraterrestrial coronal intensity ratio" $I_{\mathrm{E}}^{\mathrm{C}}(\lambda)$ measured for that pixel as described in Equation (1).

$$\frac{I_{\mathrm{E}}^{\mathrm{C}}(4100)}{I_{\mathrm{E}}^{\mathrm{C}}(3850)} = \frac{I_{\mathrm{E}}^{\mathrm{P}}(4100)/I_{\mathrm{E}}^{\mathrm{P}}(3850)}{I_{\mathrm{T}}^{\mathrm{P}}(4100)/I_{\mathrm{T}}^{\mathrm{P}}(3850)} \times \frac{I_{\mathrm{T}}^{\mathrm{C}}(4100)}{I_{\mathrm{T}}^{\mathrm{C}}(3850)}. \tag{1}$$

4. Comparison to Other Published Results

Figure 12 and Figure 13 show the temperature profiles from Figure 11 along the western coronal Equator and the southern coronal Pole along with measurements from other authors. Our results show that the temperature rise is much more rapid with coronal heights in the southern coronal Pole in comparison with the western coronal equator.

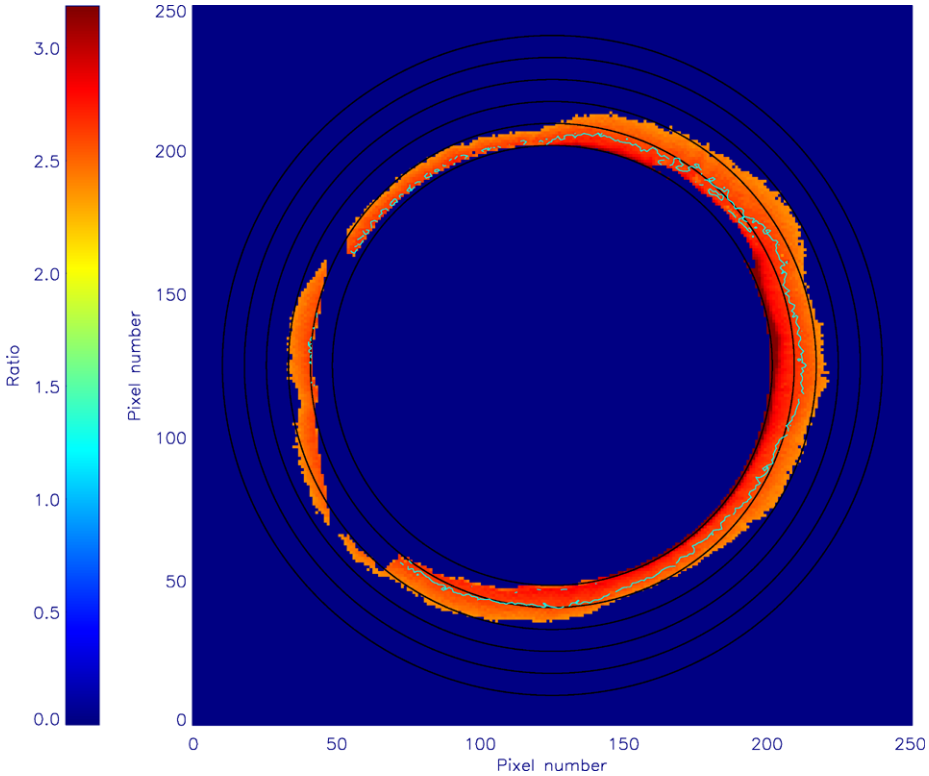

Figure 11 "Extraterrestrial coronal intensity ratios" $I_{\mathrm{E}}^{\mathrm{C}}(\lambda)$ for the 29 March 2006 totality. To determine the electron temperatures from the measured "extraterrestrial coronal intensity ratios" given by LHS of Equation (1), they have to be compared with the modeled "temperature-sensitive intensity ratios" shown in Figure 6. The contour representing "extraterrestrial coronal intensity ratio" of 2.78 corresponds to a electron temperature of 1.0 MK in the coronal plasma. The dark regions with zero ratio represents the Moon's shadow, overexposed pixels and pixels that have a noise level of $> 1.0\%$.

Habbal, Esser, and Arndt (1993), using extreme ultraviolet (EUV) observations made simultaneously in three spectral lines at the limb of a polar coronal hole, have found temperatures of $0.78-0.93$ MK between $1.02-1.07\,R_{\odot}$. They have emphasized that even with the most ideal circumstance they could not have determined the temperatures with an accuracy better than 20%. Tu *et al.* (1998), using the EUV lines based on ions and measured by *Solar Ultraviolet Measurements of Emitted Radiation* (SUMER) instrument on SOHO, have determined temperatures of $1.3-5.0$ MK in the region $1.02-1.06\,R_{\odot}$. Marsch *et al.* (1999), using the *Ultraviolet Coronagraph Spectrometer* (UVCS) in addition to EUV on SOHO, have measured temperatures of $0.09-0.2$ MK at $1.2\,R_{\odot}$, and Marsch, Tu, and Wilhelm (2000) have measured hydrogen temperature gradients of $0.1-0.2$ MK at the limb of the northern coronal hole. David *et al.* (1998), using the *Coronal Diagnostic Spectrometer* (CDS) and SUMER on SOHO, have determined electron-temperature gradients of 0.8 MK around the limb, rising to a maximum of 1.0 MK at $1.5\,R_{\odot}$, then falling to around 0.4 MK at $1.3\,R_{\odot}$. In an empirical study, Ko *et al.* (1997) have stated that the electron temperature profile should have a maximum temperature within $2.0\,R_{\odot}$. This is based on the notion that solar wind ions flowing outward through the solar corona generally have their ionic fractions "freeze-in" within $5.0\,R_{\odot}$. Accordingly, their results produce a temperature maximum (T_{Max})

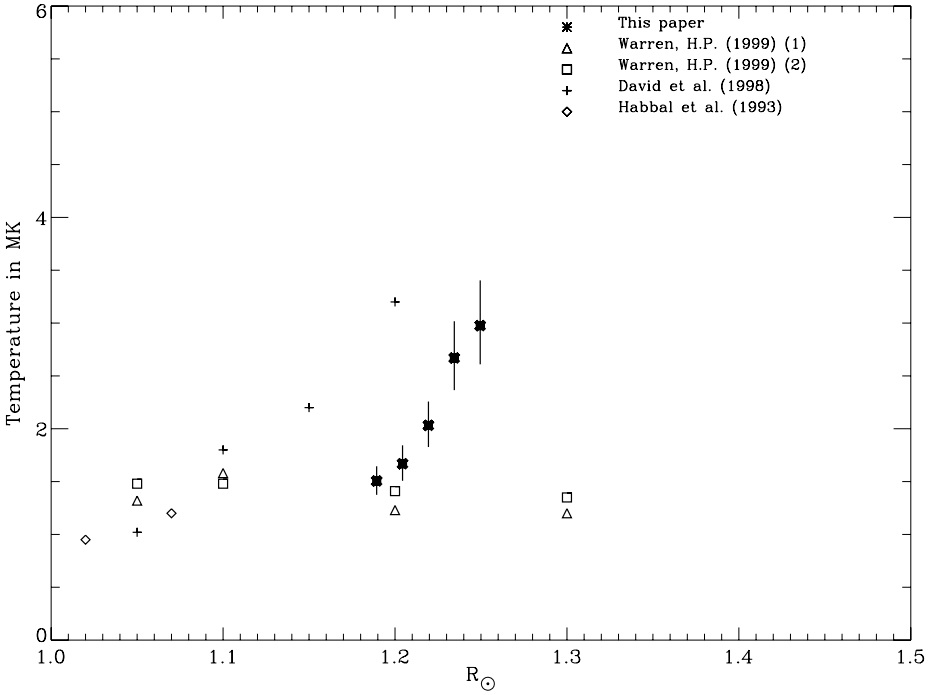

Figure 12 Electron-temperature profile along the western coronal Equator in Figure11.

of 1.5×10^6 K $\leq T_{\rm Max} \leq 1.6 \times 10^6$ K with the location of the temperature maximum ($R_{\rm Max}$) within $1.3 R_\odot \leq R_{\rm Max} \leq 1.5 R_\odot$. Fisher and Guhathakurta (1995) using the white-light coronal observations from the Spartan 201-01 spacecraft and the ground-based K-coronameter at Mauna Loa, Hawaii have determined coronal temperatures of 0.75 – 1.0 MK at coronal heights extending from $1.2 - 1.5 R_\odot$. Warren (1999) measured the electron temperature using data from SUMER and the *Transition Region and Coronal Explorer* (TRACE) and using the ionization balances of Arnaud and Raymond (1992) and Arnaud and Rothenflug (1985), which are shown as Warren (1999) (1) and (2) in Figure 12, respectively.

5. Discussion

This technique provides the capability to produce electron-temperature maps of the solar corona, which would be very useful in understanding coronal dynamics and setting the innermost boundary conditions for interplanetary-medium models. Unfortunately, a totality only provides a limited duration for any kind of measurements and limits our focus to the low solar-coronal regions. With greater coronal heights, the F-coronal signal would become significant and would require the use of polarizers to remove its contribution, which is not feasible with the short durations of the totalities. Although a ground-based coronagraph would overcome this time constraint, it will introduce the sky background, which could be removed through the use of polarizers due to the non-polarized nature of the sky. In this regard we are in the process of experimenting with this technique using the *Solar-C* coronagraph located at the Mees Solar Observatory in Haleakala, Hawaii (Kuhn *et al.*, 2003). However, a space-based coronagraph would eliminate the introduction of sky brightness.

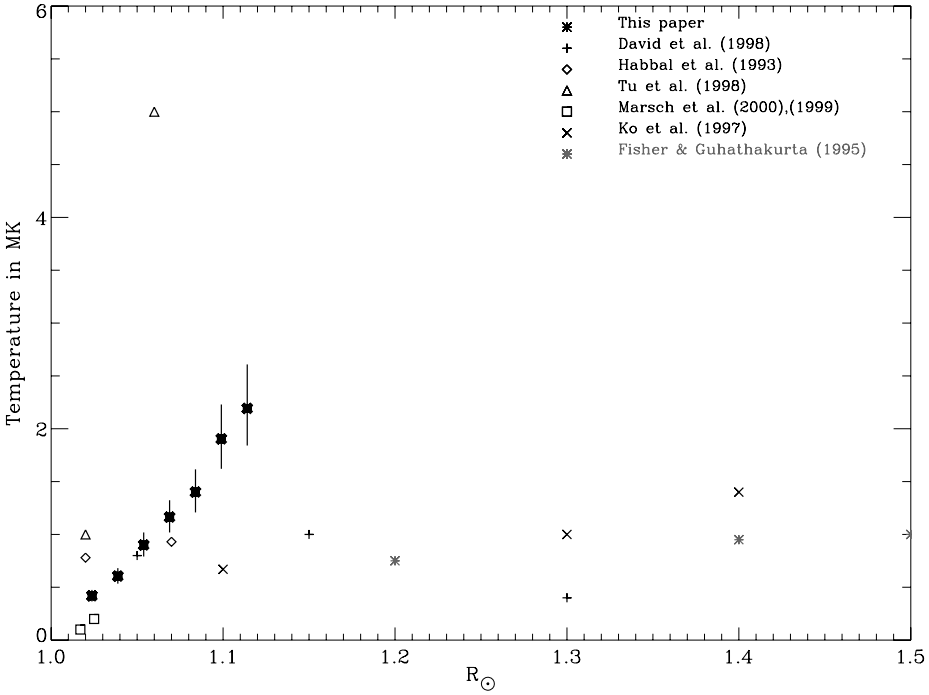

Figure 13 Electron-temperature profile along the southern coronal Pole in Figure 11.

This technique could also be used in mapping the electron flow speeds through the use of filters centered at 3987 Å and 4233 Å which is described in Reginald and Davila (2000). However, here the requirements are more demanding with a noise level of 1% yielding an uncertainty of ± 200 km s^{-1} on the electron bulk flow speed measurements. Nevertheless, with current improvement in technology we should be able to improve upon that noise level.

We would also like to emphasize that these measurement of the coronal electron temperature are based on electrons, which are the lightest particles in the corona. Also the only atomic constant that is required in the modeling is the Thomson-scattering cross section, which has been quantified to a very high degree of accuracy. Since the coronal measurements described in this paper are subject to electron-based physics, it would be then interesting to compare these same measurements obtained from ion-based physics. This would enable us to ascertain whether these two types of measurements complement each other.

Another important coronal parameter that is required for the modeling is the electron-density distribution along the line of sight. A study was made on the effects of using different electron-density models found in the literature on the shape of the K-coronal spectrum. This work was presented in Reginald, Davila, and St. Cyr (2004) and it was concluded that the differences in the shapes were insufficient to alter the results. In this respect we can measure the electron-density distribution at the time of the experiment by the measurement of the coronal polarized brightness at three polarization angles. In the context of an eclipse the only constraint that hinders this effort is the observation time. Thus having a space-based ISCORE integrated on to a coronagraph would easily yield all of these three measurements, namely the electron density, electron temperature, and electron bulk flow speed.

Acknowledgements We acknowledge Jonathan Nickerson from the University of Colorado who spent the Summer of 2007 and helped us with the calibration work. We also acknowledge the invitation extended to us by the Libyan Government through Minister Matoug Matoug and for the coordination of all of the logistical issues through Dr. Hadi Gashut, Director, Libyan National Bureau for Research and Development and the efforts of Diana A. McCeffrey of the United States Department of State and staff at the Unites States Embassy in Libya.

References

Arnaud, M., Raymond, J.: 1992, *Astrophys. J.* **398**, 394.
Arnaud, M., Rothenflug, R.: 1985, *Astron. Astrophys. Suppl. Ser.* **60**, 425.
Baumbach, S.: 1937, *Astron. Nachr.* **263**, 121.
Brosius, J.W., Davila, J.M., Thomas, R.J., Saba, J.L.R., Hara, H., Monsignori-Fossi, B.C.: 1997, *Astrophys. J.* **477**, 969.
Brueckner, G.E., Howard, R.A., Koomen, M.J., Korendyke, C.M., Michels, D.J., Moses, J.D., Socker, D.G., Dere, K.P., Lamy, P.L., Llebaria, A., Bout, M.V., Schwenn, R., Simnett, G.M., Bedford, D.K., Eyles, C.J.: 1995, *Solar Phys.* **162**, 357.
Cram, L.S.: 1976, *Solar Phys.* **48**, 3.
David, C., Gabriel, A.H., Bely-Dubau, F., Fludra, A., Lemaire, P., Wilhelm, K.: 1998, *Astron. Astrophys.* **336**, L90.
Espenak, F., Anderson, J.: 2004, *Total Solar Eclipse of 2006 March 29 NASA/TP-2004-212762*, NASA, Washington.
Fineschi, S., Gardner, L.G., Kohl, J.L., Romoli, M., Noci, G.: 1998, *Proc. SPIE XUV Astron. Obs. Missions Payloads* **3443**, 67.
Fisher, R., Guhathakurta, M.: 1995, *Astrophys. J.* **447**, L139.
Grall, R.R., Coles, W.A., Klinglesmith, M.T., Breen, A.R., Williams, P.J.S., Markannen, J., Esser, R.: 1996, *Nature* **379**, 429.
Guhathakurta, M., Fisher, R.R., Altrock, R.C.: 1993, *Astrophys. J.* **414**, L145.
Habbal, S., Esser, R., Arndt, M.B.: 1993, *Astrophys. J.* **413**, 435.
Ichimoto, K., Kumagai, K., Sano, I., Kobiki, T., Sakurai, T., Munoz, A.: 1996, *Publ. Astron. Soc. Japan* **48**, 545.
Ko, Y.K., Geiss, J., Gloeckler, G., Guhathakurta, M.: 1997, *Solar Phys.* **171**, 345.
Kohl, J.L., Esser, R., Gardner, L.D., Habbal, S., Daigneau, P.S., Dennis, E.F., Nystrom, G.U., Panasyuk, A., Raymond, J.C., Smith, P.L., Strachan, L., van Ballegooijen, A.A., Noci, G., Fineschi, S., Romoli, M., Ciaravella, A., Modigliani, A., Huber, M.C.E., Antonucci, E., Benna, C., Giordano, S., Tondello, G., Nicolosi, P., Naletto, G., Pernechele, C., Spadaro, D., Poletto, G., Livi, S., von der Lühe, O., Geiss, J., Timothy, J.G., Gloeckler, G., Allegra, A., Basile, G., Brusa, R., Wood, B., Siegmund, O.H.W., Fowler, W., Fisher, R., Jhabvala, M.: 1995, *Solar Phys.* **162**, 313.
Kuhn, J.R., Coulter, R., Lin, H., Mickey, D.L.: 2003, *Proc. SPIE Innov. Telesc. Instrum. Solar Astrophys.* **4853**, 318.
Kurucz, R.L., Furenlid, I., Brault, J., Testerman, L.: 1984, *Solar Flux Atlas from 296 nm to 1300 nm*, National Solar Observatory, Arizona.
Marsch, E., Tu, C.Y., Heinzel, P., Wilhelm, K., Curdt, W.: 1999, *Astron. Astrophys.* **347**, 676.
Marsch, E., Tu, C.Y., Wilhelm, K.: 2000, *Astron. Astrophys.* **359**, 381.
Mason, H.E., Young, P.R., Pike, C.D., Harrison, R.A., Fludra, A., Bromage, B.J.I., del Zanna, G.: 1997, *Solar Phys.* **170**, 143.
November, L., Koutchmy, S.: 1996, *Astrophys. J.* **466**, 512.
Reginald, N.L.: 2000, Ph.D. thesis, University of Delaware.
Reginald, N.L., Davila, J.M.: 2000, *Solar Phys.* **195**, 111.
Reginald, N.L., Davila, J.M., St. Cyr, O.C.: 2004, *Solar Phys.* **225**, 249.
Reginald, N.L., St. Cyr, O.C., Davila, J.M., Brosius, J.W.: 2003, *Astrophys. J.* **599**, 596.
St. Cyr, O.C., Davila, J.M., Guhathakurta, M., Senseney, R.: 2007, *EoS, Trans. Am. Geophys. Union* **88**, 539.
Strachan, L., Kohl, J.L., Weiser, H., Withbroe, G.L., Munro, R.H.: 1993, *Astrophys. J.* **412**, 410.
Tu, C.Y., Marsch, E., Wilhelm, K., Curdt, W.: 1998, *Astrophys. J.* **503**, 475.
Warren, H.P.: 1999, *Solar Phys.* **190**, 363.